


# SENSORLESS DTC BASED ON ARTIFICIAL NEURAL NETWORK FOR INDEPENDENT CONTROL OF DUAL 5-PHASE INDUCTION MACHINE FED BY A THREE-LEVEL NPC INVERTER

Khaled Mohammed Said BENZAOU<sup>1</sup> , Elakhdar BENYOUSSEF<sup>1</sup> ,  
Sifelislam GUEDIDA<sup>2,\*</sup> , Bekheira TABBACHE<sup>2</sup> , Ahmed Zouhir KOUACHE<sup>1</sup> 

<sup>1</sup>Faculté des Sciences Appliquées, Laboratoire LAGE, Univ Ouargla, Ouargla 30 000, ALGERIE

<sup>2</sup>UER ELT, Ecole Militaire Polytechnique, 16111 Algiers, Algeria

benzaoui.khaled@univ-ouargla.dz, lakhdarbenyoussef@yahoo.com, guedida.sifelislam@gmail.com,  
bekheira.tabbache@emp.mdn.dz, Kouache.ahmed@univ-ouagla.dz

\*Corresponding author: Sifelislam GUEDIDA; guedida.sifelislam@gmail.com

DOI: 10.15598/aece.v22i3.5738

Article history: Received Feb 04, 2024; Revised Jun 24, 2024; Accepted Jul 03, 2024; Published Sep 30, 2024.

This is an open access article under the BY-CC license.

**Abstract.** *This paper deals with an independent control of two parallel-connected five-phase induction machines (FPIM) fed by NPC three-level inverter. In effect a direct torque control (DTC) of two parallel-connected FPIMs has been developed to ensure a simple and fast decoupled control over the stator flux and electromagnetic torque and high performance in event of machine parameters disturbances. However, DTC suffer from the torque and flux ripples due the hysteresis controllers. In this context, an intelligent DTC based on Artificial Neural Network (ANN) has been proposed to minimize the stator flux and electromagnetic torque ripples in a steady and transient states and therefore reduction of the stator current harmonic THD. hence, Intelligent ANN hysteresis controllers and switching table of the DTC have been incorporated to select the optimum voltage vector of the NPC-VSI to be applied in the control of two parallel-connected FPIM. Moreover, a virtual current sensor (VCS) approach is proposed to configure a fault-tolerant control scheme (FTC). The effectiveness of the proposed (DTC-ANN) and the FTC have been checked by an intensive simulation in different operating conditions.*

## Keywords

*Two-machine parallel connected drive, direct torque control (DTC), five-phase induction machine (FPIM), artificial neural network (ANN), fault-tolerant control (FTC), virtual current sensor (VCS).*

## 1. Introduction

Regarding to reliability, reduced cost and high performance, AC machines drives are widely used in industrial applications such as: EV traction, ship propulsion systems, pump extruder, and locomotive traction. Thus, many papers are interested in multiphase AC machine drives, particularly five-phase induction machines (FPIM), due to the improved magnetic motive force (MMF) waveforms, high efficiency, lower losses, and torque enhancement. Moreover, the FPIM presents a promising solution in fault-tolerant operation [1–3].

Generally, the FPIMs are fed by a single voltage source inverter (VSI). For two parallel-connected FPIMs, one voltage source inverter (VSI) can ensure independent control. The vector control scheme uses only two current components while using the remaining

components, resulting from harmonic components, to control the other machine with a proper phase transposition [4–8]. However, vector control suffers from machine parameter variations.

In term of power electronics, power inverters are the most crucial part of AC machine drives because of their wide operating range. However, conventional two-level inverters are limited, especially in high-power applications. The three-level neutral-point-clamped (TL-NPC) inverter is the most widely accepted multi-level topology for high-power and medium-voltage applications due to its inherent advantages, such as low stress on power semiconductor switches and low total harmonic distortion in current and voltage [9]. Due to these advantages, TL-NPC inverters are also suitable for multiphase machine drives. Various studies have been reported in the literature for five-phase induction machine drives based on the TL-NPC inverter to provide better power quality and increased efficiency. These characteristics make them suitable for adjustable-speed drives. Regarding to these advantages, this paper proposes the three-level neutral-point-clamped (TL-NPC) to feed the two-machine FPIM parallel connected drive.

In this context, the direct torque control DTC can be providing decoupled flux and torque control of the IM with high performance [10]. For this, hysteresis controllers (HCs) are used [11]. Thus, the electromagnetic torque and stator flux are kept in their predefined hysteresis bands (HB). Nevertheless, the stator flux and electromagnetic torque present more ripples caused by the non-linear nature of the used HCs which lead to higher harmonic content and mechanical vibration [11], [12] and [13].

Consequently, several techniques were investigated to enhance the DTC by integrating artificial neural networks (ANN) to replace the hysteresis controllers (HCs) and the switching table (ST) [14–18]. Thus, the ANN approach allows the optimum selection of the voltage vector (VV) applied to the FPIM to ensure a high dynamic response, significantly reduce the electromagnetic torque and flux ripples, and, therefore, minimize the stator current harmonic.

On the other hand, sensorless and fault-tolerant control (FTC) for AC machines has become more recommended in the literature due to hazardous operating conditions that lead to current (CS) and speed sensor failures, the most frequent type of failure for measurement equipment. This latter can deteriorate the performance of any vector control scheme, causing a loss of accurate measurements of the state variables, the stator flux, and electromagnetic torque [19].

The current sensor fault tolerant control (CS-FTC) strategies in the literature can be grouped into hardware and software solutions. Nevertheless, the first so-

lution whose functionality is based on the redundancy of the CS or implementing additional equipment, i.e., shunt resistor [20, 21], is associated with higher complexity, size, and cost [19]. On the other hand, software solutions for current reconstruction are more attractive, and a virtual current sensor (VCS) can be implemented to replace the CS [22, 23]. The VCS algorithm is based on the machine model and DC link voltage measurement [19]. Furthermore, the DTC relies on an open-loop estimator for the state variables estimation. However, this latter especially during low-speed operation suffers from integration problems. Therefore, several sensorless control schemes have been developed to tackle the aforementioned drawback such as sliding mode observer [24], model reference adaptive system [25], and extended Kalman filter [6]. In this paper, a simple method is discussed based on the reconstructed stator currents, the machine's state variables, stator flux, electromagnetic torque, and rotor speed, can be estimated, ensuring a complete sensorless control for post-fault operation.

In this context, this paper presents FTC sensorless ANN-based direct torque control DTC-ANN for two parallel-connected FPIMs with a machine's state variables reconstruction method. The developed control can improve the stator flux and electromagnetic torque performance in a steady and transient state, reduce the stator flux and electromagnetic torque ripples and ensure a fault-tolerant control operation in event of current sensor failure.

In this paper, the developed control is structured in the following section: 1) mathematical modelling of the developed system, 2) independent DTC of the dual-machine, 3) intelligent DTC based on artificial neural networks scheme, 4) sensorless control and 5) results validation.

## 2. Parallel connected multi-machine drive modelling

Figure 1 illustrates the diagram of the two parallel-connected five phase induction motors (FPIMs) drive. The topology of the power converter is a three-level voltage source inverter (THL-VSI) with 243 ( $3^5$ ) possible sequence combinations (240 active and three zeros VVs) [24]. The switching function for these VVs is denoted by  $S = [S_A, S_B, S_C, S_D, S_E]^T$ , where  $S_i = 2$  or 0 or 1, as state 2 denotes switching "ON" of the two upper semiconductor switches ( $S_{A1,2}, S_{B1,2}, S_{C1,2}, S_{D1,2}$  &  $S_{E1,2}$ ). On the other hand, state 0 denotes turning "ON" the two lower switches ( $S_{A3,4}, S_{B3,4}, S_{C3,4}, S_{D3,4}$  &  $S_{E3,4}$ ); meanwhile, state 1 denotes turning "ON" only the two mid-

dle switches ( $S_{A2,3}, S_{B2,3}, S_{C2,3}, S_{D2,3}$  &  $S_{E2,3}$ ). The expression of the pole voltage to the midpoint of the dc-link for phase A as an example is:

$$V_{AZ} = \frac{S_A - 1}{2} V_{dc}, \quad (1)$$

As for the phase voltages to the neutral point are expressed as:

$$\begin{bmatrix} V_{AN} \\ V_{BN} \\ V_{CN} \\ V_{DN} \\ V_{EN} \end{bmatrix} = \frac{2}{5} \begin{bmatrix} 4 & -1 & -1 & -1 & -1 \\ -1 & 4 & -1 & -1 & -1 \\ -1 & -1 & 4 & -1 & -1 \\ -1 & -1 & -1 & 4 & -1 \\ -1 & -1 & -1 & -1 & 4 \end{bmatrix} \begin{bmatrix} V_{AZ} \\ V_{BZ} \\ V_{CZ} \\ V_{DZ} \\ V_{EZ} \end{bmatrix}, \quad (2)$$

The following formulas map the VVs represented by their switching combinations into and subspaces (see Fig. 2) [5]:

$$\begin{aligned} V_{\alpha\beta 1}^{inv} &= \frac{2}{5} (V_{AN}^{inv} + V_{BN}^{inv} e^{j2\pi/5} + V_{CN}^{inv} e^{j4\pi/5} \\ &\quad + V_{DN}^{inv} e^{j6\pi/5} + V_{EN}^{inv} e^{j8\pi/5}) \\ V_{\alpha\beta 2}^{inv} &= \frac{2}{5} (V_{AN}^{inv} + V_{CN}^{inv} e^{j2\pi/5} + V_{EN}^{inv} e^{j4\pi/5}, \\ &\quad + V_{BN}^{inv} e^{j6\pi/5} + V_{DN}^{inv} e^{j8\pi/5}) \end{aligned} \quad (3)$$

The two FPIMs have five windings spatially shifted by 72 electrical degrees. The zero sequence voltages are not considered since the two FPIMs are star-connected.

The phase transposition shown in Fig. 1 between the terminals of the second machine and the inverter allows for independent control of each one of the motors in the drive.

The following is the relation between the voltages and currents of the THL-VSI and the two motors:

$$V_{ABCDE} = \begin{bmatrix} V_{AN}^{inv} \\ V_{BN}^{inv} \\ V_{CN}^{inv} \\ V_{DN}^{inv} \\ V_{EN}^{inv} \end{bmatrix} = \begin{bmatrix} V_{SA1} = V_{SA2} \\ V_{SB1} = V_{SC2} \\ V_{SC1} = V_{SE2} \\ V_{SD1} = V_{SB2} \\ V_{SE1} = V_{SD2} \end{bmatrix}, \quad (4)$$

$$i_{ABCDE} = \begin{bmatrix} i_{AN}^{inv} \\ i_{BN}^{inv} \\ i_{CN}^{inv} \\ i_{DN}^{inv} \\ i_{EN}^{inv} \end{bmatrix} = \begin{bmatrix} i_{SA1} + i_{SA2} \\ i_{SB1} + i_{SC2} \\ i_{SC1} + i_{SE2} \\ i_{SD1} + i_{SB2} \\ i_{SE1} + i_{SD2} \end{bmatrix}, \quad (5)$$

For the five-phase AC machines drive, Clark's transformation matrix describes the state variables in two orthogonal subspaces and zero sequence components [5].

$$[C] = \frac{2}{5} \begin{bmatrix} 1 & \cos(\vartheta) & \cos(2\vartheta) & \cos(3\vartheta) & \cos(4\vartheta) \\ 0 & \sin(\vartheta) & \sin(2\vartheta) & \sin(3\vartheta) & \sin(4\vartheta) \\ 1 & \cos(2\vartheta) & \cos(4\vartheta) & \cos(\vartheta) & \cos(3\vartheta) \\ 0 & \sin(2\vartheta) & \sin(4\vartheta) & \sin(\vartheta) & \sin(3\vartheta) \\ 1/2 & 1/2 & 1/2 & 1/2 & 1/2 \end{bmatrix}, \quad (6)$$

where:  $\vartheta = 2\pi/5$ . By applying Clark's transformation matrix to Eq. (4) and Eq. (5), the two machines stator voltages and currents are expressed in the  $\alpha\beta 1$  and  $\alpha\beta 2$  planes as follows [8] and [25]:

$$\begin{aligned} V_{ABCDE} &= \begin{bmatrix} V_{\alpha 1}^{inv} \\ V_{\beta 1}^{inv} \\ V_{\alpha 2}^{inv} \\ V_{\beta 2}^{inv} \\ V_0^{inv} \end{bmatrix} = [C] V_{ABCDE}^{inv} = \begin{bmatrix} v_{s1\alpha 1} = v_{s2\alpha 2} \\ v_{s1\beta 1} = -v_{s2\beta 2} \\ v_{s1\alpha 2} = v_{s2\alpha 1} \\ v_{s1\beta 2} = -v_{s2\beta 1} \\ 0 \end{bmatrix}, \\ \text{and} \\ i_{ABCDE} &= \begin{bmatrix} i_{\alpha 1}^{inv} \\ i_{\beta 1}^{inv} \\ i_{\alpha 2}^{inv} \\ i_{\beta 2}^{inv} \\ i_0^{inv} \end{bmatrix} = [C] i_{ABCDE}^{inv} = \begin{bmatrix} i_{s1\alpha 1} + i_{s2\alpha 2} \\ i_{s1\beta 1} - i_{s2\beta 2} \\ i_{s1\alpha 2} + i_{s2\alpha 1} \\ i_{s1\beta 2} + i_{s2\beta 1} \\ 0 \end{bmatrix}, \end{aligned} \quad (7)$$

The obtained model of each of the FPIM in the stationary reference frame, under the same assumptions as the three-phase machine, is as follows [8, 27]:

$$\begin{cases} v_{s1\alpha\beta 1}^{inv} = R_{s1} i_{s1\alpha\beta 1} + L_{s1} \frac{di_{s1\alpha\beta 1}}{dt} + L_{m1} \frac{di_{r1}}{dt} \\ \quad = R_{s2} i_{s2\alpha\beta 2} + L_{s1} \frac{di_{s2\alpha\beta 2}}{dt} \\ v_{s2\alpha\beta 2}^{inv} = R_{s2} i_{s2\alpha\beta 2} + L_{s2} \frac{di_{s2\alpha\beta 2}}{dt} + L_{m2} \frac{di_{r2}}{dt} \\ \quad = R_{s1} i_{s1\alpha\beta 1} + L_{s1} \frac{di_{s1\alpha\beta 1}}{dt} \\ 0 = R_{rx} i_{rx} + L_{rx} \frac{di_{rx}}{dt} + L_{mx} \frac{di_{sx\alpha\beta x}}{dt} - j\omega(L_{mx} i_{sx\alpha\beta x} + L_{rx} i_{rx}) \end{cases}, \quad (8)$$

It is clear that the model obtained for each of the FPIMs in the stationary reference frame is under the same assumptions as the three-phase motor.

In addition, the expression of the stator flux linkages, module, and position:

$$\begin{cases} \phi_{sx\alpha\beta x} = \int (v_{sx\alpha\beta x} - R_{sx} i_{sx\alpha\beta x}) dt \\ \phi_{sx} = \sqrt{\phi_{sx\alpha\alpha}^2 + \phi_{sx\beta\beta}^2} \\ \theta_{sx} = \tan^{-1}(\frac{\phi_{sx\beta\beta}}{\phi_{sx\alpha\alpha}}) \end{cases}, \quad (9)$$

The electromagnetic torque expression:

$$T_{emx} = \frac{5P_x}{2} (\phi_{sx\alpha\alpha} i_{sx\beta\beta} - \phi_{sx\beta\beta} i_{sx\alpha\alpha}), \quad (10)$$

The mechanical equations:

$$j_x \frac{d\omega_{mx}}{dt} = T_{emx} - T_{Lx} - f_x \omega_{mx}, \quad (11)$$

Where:  $x =$  (Machine 1 or Machine 2),  $V_{s\alpha\beta j}$  stator voltages,  $i_{s\alpha\beta j}$  stator currents,  $\phi_{s\alpha}, \phi_{s\beta}$  stator flux linkages,  $i_r$  rotor currents,  $R_s$  stator resistance,  $L_{sl}$  stator leakage inductance,  $L_m$  mutual inductance,  $R_r$  rotor resistance,  $\omega$  rotor electrical speed,  $\omega_m$  rotor mechanical speed,  $T_{em}$  electromagnetic torque,  $T_L$  load torque,  $p$  pair poles,  $J$  moment of inertia,  $f$  viscous friction coefficient.

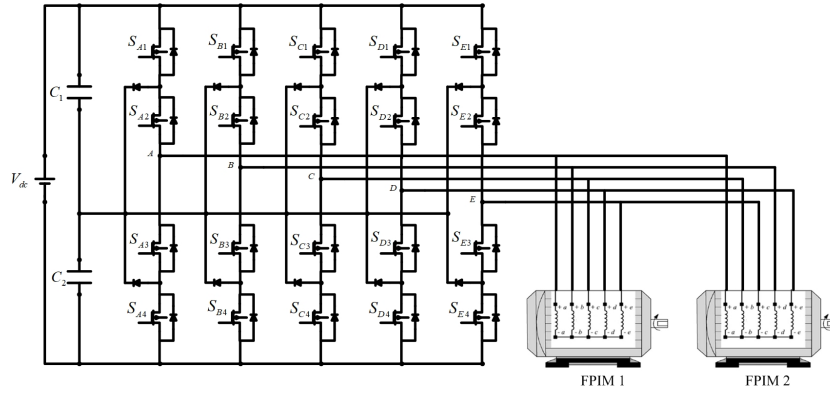


Fig. 1: Circuit topology of two symmetrical FPIM Parallel connected fed by single THL-VSI.

### 3. Direct torque control

Figure 3 illustrates the schematic diagram of the DTC algorithm used to control the two-machine drive. The DTC algorithm exploits the laws of instantaneous space vector theory to achieve the desired control over the machine’s stator flux and electromagnetic torque [11]. Two distinct DTC controllers are used for each FPIM to maintain independent control over the two-machine drive and the decoupling between the stator flux and electromagnetic torque.

As stated above, the primary working principle of DTC lies in selecting the optimal VV to meet the stator flux and electromagnetic torque requirements following four steps. The two first steps are identical for the two machines:

#### 3.1. Stator flux and electromagnetic torque estimation

Based on the stator voltage model of the FPIM in the stationary reference frame, the stator flux linkages component, module, and position are expressed as follows:

$$\begin{cases} \hat{\phi}_{sx\alpha\beta x} = \int (v_{s\alpha\beta x} - R_{sx}i_{sx\alpha\beta x}) dt \\ \hat{\phi}_{sx} = \sqrt{\hat{\phi}_{sx\alpha\alpha}^2 + \hat{\phi}_{sx\beta\beta}^2} \\ \hat{\theta}_{sx} = \tan^{-1}\left(\frac{\hat{\phi}_{sx\beta\beta}}{\hat{\phi}_{sx\alpha\alpha}}\right) \end{cases}, \quad (12)$$

The FPIM’s produced electromagnetic torque can be expressed by the cross product of the stator flux and currents components as follows:

$$\hat{T}_{emx} = \frac{5P_x}{2}(\hat{\phi}_{sx\alpha\alpha}i_{sx\beta\beta} - \hat{\phi}_{sx\beta\beta}i_{sx\alpha\alpha}), \quad (13)$$

#### 3.2. Hysteresis Controllers (HC)

This step compares the control commands and estimated values of the stator flux and electromagnetic

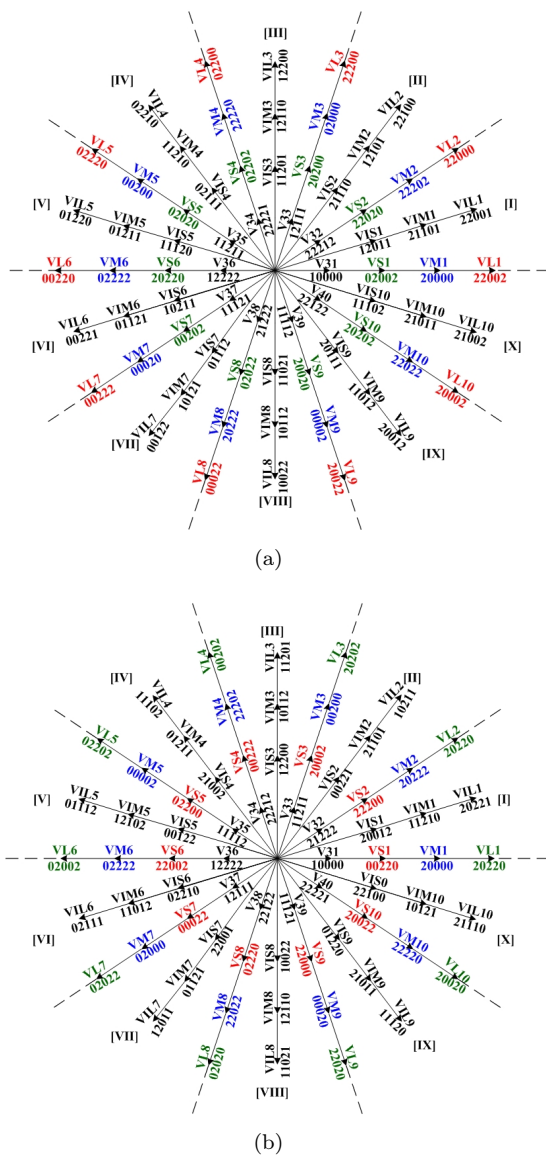


Fig. 2: Voltage Vectors of the three Level-voltage source inverter: (a) VVs mapped in  $\alpha\beta 1$  plan and (b) VVs mapped in  $\alpha\beta 2$  plan.



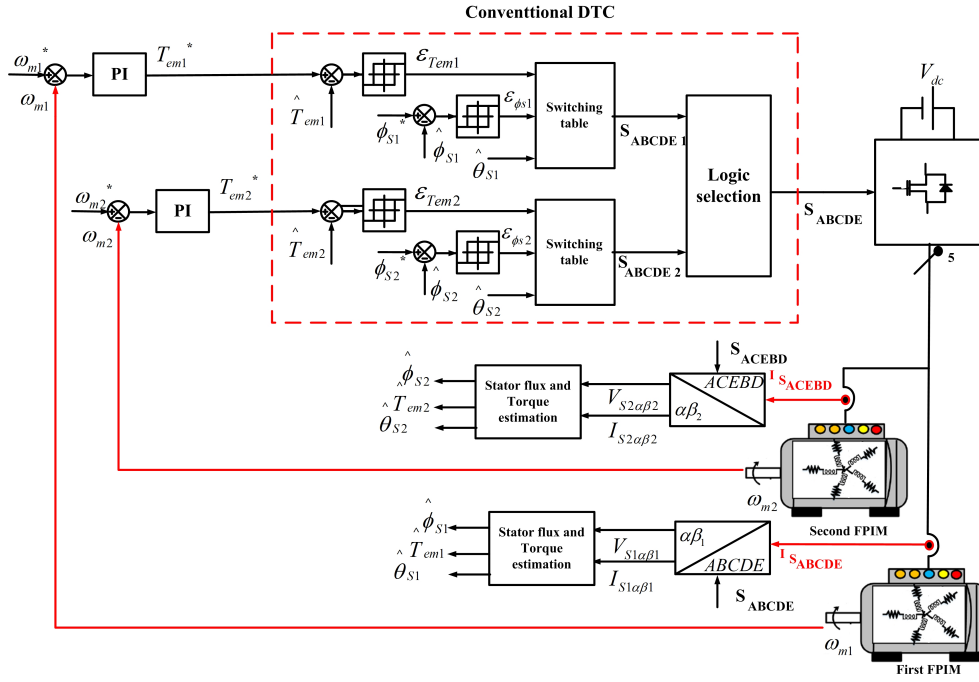
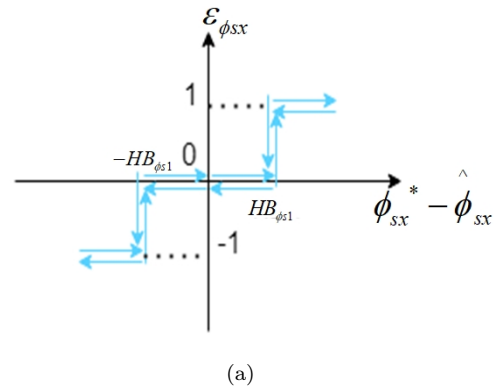


Fig. 3: Schematic diagram of three-level DTC for two parallel-connected FPIMs.

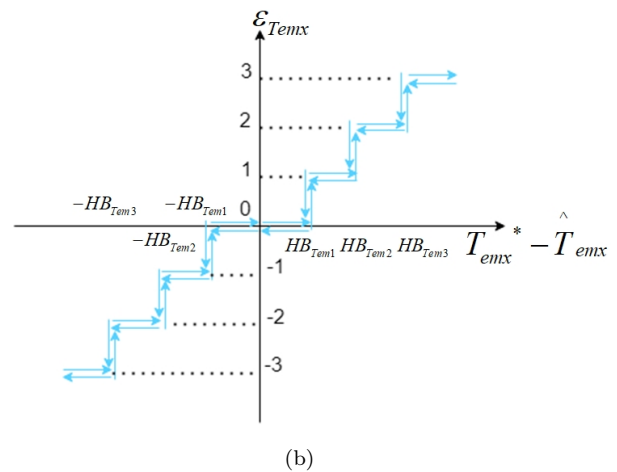
torque. Figure 4(a) illustrates the structure of the two-level HC utilized for the stator flux, where the error between the reference  $\phi_{sx}^*$  and estimated  $\hat{\phi}_{sx}$  values is the input of the HC, and the digital output of this controller is the required action on the stator flux of the FPIM proportional to the predefined HB. As for the electromagnetic torque, the implemented seven-level HC is shown in Fig. 4(b), where the error between the reference  $T_{emx}^*$  and estimated  $\hat{T}_{emx}$  values is the input of the HC, and the output of this latter is the required action on the machine torque proportional to the predefined HB [26].

### 3.3. Switching table

According to the applied phase transposition in the parallel connection of the drive placing the  $\alpha\beta$  axis windings of the FPIM2 into the  $\alpha\beta 2$  of the THL-VSI. While the first FPIM  $\alpha\beta$  axis windings are placed into the  $\alpha\beta 1$  plane. Hence, an independent vector control over the two FPIMs based on DTC scheme can be achieved; where the difference lies with the developed ST. The ST for the first FPIM's control scheme exploits the  $\alpha\beta 1$  plane VVs of the THL-VSI and  $\alpha\beta$  plane VVs for the second FPIM, ensuring a current components producing flux and torque for the first machine and non-generating for the second machine and vice versa. i.e., if the stator flux of the FPIM1 lies in sector VIII and the flux and torque must be increased ( $\epsilon_{\phi_{sx}} = 1, \epsilon_{T_{emx}} = 2$ ) the applied VV is VM9 with a switching sequence of 00002 from Figure 2(a). Moreover, if the flux of the FPIM2 needs to be de-



(a)



(b)

Fig. 4: Structure of the implemented HCs: (a) Two-level HC (b) Seven-level HC.

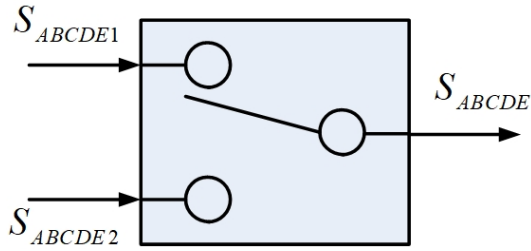


**Fig. 5:** Logic selection block.

created ( $\varepsilon_{\phi_{sx}} = -1$ ) and the torque to be increased ( $\varepsilon_{T_{emx}} = 3$ ) while the stator flux is in sector V, the selected VV is VL9 with a sequence of 22020 from Figure 2(b).

### 3.4. Logic selection

The structure of the logic selection block is illustrated in Fig. 5. For each sampling period, the two DTC controllers select the appropriate VV to be applied, and the logic selection block chooses which VV to apply to the THL-VSI for each of them for one sampling period alternatively. For example, if the VM9 and VL9 are selected for the FPIM1 and FPIM2, respectively, the block will apply the VM9 for one sampling period then the VL9 for the second period, and so on.

## 4. Artificial neural network-based DTC

The artificial neurons are the cornerstone components of the ANN. These computational elements are the non-linear mathematical model of the human biological neurons as follows [3]:

$$\begin{cases} y_i = F_1(s) \left\{ \sum_{i=1}^N (x_i * w_i + b) \right\} \\ o_i = F_2(s) \left\{ \sum_{i=1}^N (x_i * w_i + b) \right\} \end{cases}, \quad (14)$$

Where:  $x_i$  are the neuron input signals,  $w_i$  the neuron weight, bias parameter, the output of the neuron, and  $F_1(s)$ ,  $F_2(s)$  are the activation functions.

The mean square error is a parameter computed from difference between the target and output pattern of the ANNS trained using the feedforward backpropagation algorithm as follows:

$$MSE = \frac{1}{N} \sum_{i=1}^N (d_i(k) - o_i(k)), \quad (15)$$

Where:  $o_i$  the ANN output,  $d_i$  the target output, the number of the training data set, and the number of iterations.

In each iteration, the neurons weights are updated to reduce the value of the cost function (MSE):

$$w_{ji}(k+1) = w_{ji}(k) - \eta \frac{\partial MSE(k)}{\partial w_{ji}(k)}, \quad (16)$$

Where:  $w_{ji}(k+1)$  the updated weight,  $w_{ji}(k)$  the previous weight, and  $\eta$  the learning rate.

The DTC scheme, recognized for its simple structure, robustness to the machine's parameter variations, and faster dynamic response, suffers from influential drawbacks that affect its performance. The stator flux and electromagnetic torque are examples of these drawbacks, where the primary cause lies in using the HCs [27]. Therefore, an AI technique based on ANN is proposed to overcome the aforementioned drawbacks.

The ANNs can approximate and further enhance the performance of most systems without the need for a precise mathematical model based on a series of training data sets [14]. Therefore, this manuscript proposes three controllers based on ANNs for the stator flux HC (ANN-HC $_{\phi_s}$ ), electromagnetic torque HC (ANN-HC $_{T_{em}}$ ), and ST (ANN-ST) are proposed; Figure 6 depicts the structure of the three ANN controllers.

Figure 7 illustrates the workflow diagram used in the training process of the three ANN controllers [14]. A supervised training method based on the backpropagation algorithm is used in the present study.

Table 2 summarizes the proposed three ANN controllers' parameters. Figure 8 shows the overall scheme of the drive where the ANN has replaced the conventional stator flux and electromagnetic torque HCs and the ST to improve the control scheme performance. The rest of the drive system is identical to the DTC scheme shown in Fig. 3.

## 5. Fault-tolerant sensorless control

As shown in Figure 5, the DTC of the two-machine drive requires a set of current sensors and encoders providing a critical feedback signal to ensure optimum performance. Thus, this study proposes a model-based FTC for current and speed sensor failure. Figure 9 presents the discussed FTC block diagram.

### 5.1. Virtual current sensor

Real time information and measurements of the stator currents are essential for the closed-loop control of ASD [19]. Therefore, the adopted approach reconstructs the five-phase currents based on the switching sequence of the THL-VSI and the measured DC link voltage using

Tab. 1: Switching table for the DTC.

| $\varepsilon_{\phi_{sx}}$ | $\varepsilon_{T_{emx}}$ | Sectors |      |       |      |     |      |       |        |      |     |
|---------------------------|-------------------------|---------|------|-------|------|-----|------|-------|--------|------|-----|
|                           |                         | [I]     | [II] | [III] | [IV] | [V] | [VI] | [VII] | [VIII] | [IX] | [X] |
| 1                         | 3                       | VL2     | VL3  | VL4   | VL5  | VL6 | VL7  | VL8   | VL9    | VL10 | VL1 |
|                           | 2                       | VM2     | VM3  | VM4   | VM5  | VM6 | VM7  | VM8   | VM9    | VM10 | VM1 |
|                           | 1                       | VS2     | VS3  | VS4   | VS5  | VS6 | VS7  | VS8   | VS9    | VS10 | VS1 |
|                           | 0                       | V0      | V0   | V0    | V0   | V0  | V0   | V0    | V0     | V0   | V0  |
|                           | -1                      | VS10    | VS1  | VS2   | VS3  | VS4 | VS5  | VS6   | VS7    | VS8  | VS9 |
|                           | -2                      | VM10    | VM1  | VM2   | VM3  | VM4 | VM5  | VM6   | VM7    | VM8  | VM9 |
|                           | -3                      | VL10    | VL1  | VL2   | VL3  | VL4 | VL5  | VL6   | VL7    | VL8  | VL9 |
| -1                        | 3                       | VL5     | VL6  | VL7   | VL8  | VL9 | VL10 | VL1   | VL2    | VL3  | VL4 |
|                           | 2                       | VM5     | VM6  | VM7   | VM8  | VM9 | VM10 | VM1   | VM2    | VM3  | VM4 |
|                           | 1                       | VS5     | VS6  | VS7   | VS8  | VS9 | VS10 | VS1   | VS2    | VS3  | VS4 |
|                           | 0                       | V0      | V0   | V0    | V0   | V0  | V0   | V0    | V0     | V0   | V0  |
|                           | -1                      | VS7     | VS8  | VS9   | VS10 | VS1 | VS2  | VS3   | VS4    | VS5  | VS6 |
|                           | -2                      | VM7     | VM8  | VM9   | VM10 | VM1 | VM2  | VM3   | VM4    | VM5  | VM6 |
|                           | -3                      | VL7     | VL8  | VL9   | VL10 | VL1 | VL2  | VL3   | VL4    | VL5  | VL6 |

Tab. 2: Characteristic details of the proposed ANN controllers.

| ANN controller parameters    |              | Methods and values details  |                    |        |
|------------------------------|--------------|---|--------------------|--------|
|                              |              | ANN- $HC_{\phi_s}$  | ANN- $HC_{T_{em}}$ | ANN-ST |
| ANN type                     |              | Feed-forward neural network   |                    |        |
| ANN training algorithm       |              | BACKPROPAGATION   |                    |        |
| Adaptation learning function |              | Trainlm   |                    |        |
| Activation function          |              | Logsig  | Logsig             | Tansig |
| Learning rate                |              | 0.5   | 0.5                | 0.5    |
| ANN architecture             | Input layer  | 1   | 1                  | 3      |
|                              | Hidden layer | 12  | 17                 | 35     |
|                              | Output layer | 1   | 1                  | 5      |
| Training data sets           |              | The data sets, five million samples, utilized during the training process were collected from the simulation results of DTC in MATLAB environments. |                    |        |

the VCS technique even at the post fault of the CS eliminating the need for this latter.

The VCS algorithm is based on three systems' equations of the stator currents, the fundamental and harmonic components, and rotor flux components in the stationary reference frame, based on the direct measurement of the DC link voltage and rotor mechanical speed as follows:

$$\begin{cases} \frac{d}{dt} \hat{\phi}_{rx\alpha} = \frac{R_{rx}}{L_{rx}} (L_{mx} \hat{i}_{sx\alpha} - \hat{\phi}_{rx\alpha}) - \hat{\omega}_{mx} \hat{\phi}_{rx\beta} \\ \frac{d}{dt} \hat{\phi}_{rx\beta} = \frac{R_{rx}}{L_{rx}} (L_{mx} \hat{i}_{sx\beta} - \hat{\phi}_{rx\beta}) - \hat{\omega}_{mx} \hat{\phi}_{rx\alpha} \end{cases}, \quad (17)$$

$$\begin{cases} \frac{d}{dt} \hat{i}_{sx\alpha} = \frac{1}{L_{sx}\sigma_x} (V_{sx\alpha} - R_{sx} \hat{i}_{sx\alpha} - \frac{L_{mx}}{L_{rx}} \hat{\phi}_{rx\alpha}) \\ \frac{d}{dt} \hat{i}_{sx\beta} = \frac{1}{L_{sx}\sigma_x} (V_{sx\beta} - R_{sx} \hat{i}_{sx\beta} - \frac{L_{mx}}{L_{rx}} \hat{\phi}_{rx\beta}) \end{cases}, \quad (18)$$

The indirect method to calculate the start flux using the reconstructed stator currents and estimated rotor flux has the advantage of avoiding the pure integration problems of the direct method [19].

As for the harmonic components, the estimator equation is as follows:

$$\begin{cases} \frac{d}{dt} \hat{\phi}_{sx\alpha\beta} = V_{sx\alpha\beta} - R_s \hat{i}_{sx\alpha\beta} \\ \hat{i}_{sx\alpha\beta} = \frac{\hat{\phi}_{sx\alpha\beta}}{L_{sx}} \end{cases}, \quad (19)$$

## 5.2. Stator flux and rotor speed estimation

The stator flux linkages components, vector, and position, in addition to the electromagnetic torque, can be calculated based on the VCS reconstructed currents and estimated rotor flux components as follows:

$$\begin{cases} \hat{\phi}_{sx\alpha} = \frac{L_{mx}}{L_{rx}} \hat{\phi}_{rx\alpha} + \frac{L_{sx}L_{rx} - L_{mx}^2}{L_{rx}} \hat{i}_{sx\alpha} \\ \hat{\phi}_{sx\beta} = \frac{L_{mx}}{L_{rx}} \hat{\phi}_{rx\beta} + \frac{L_{sx}L_{rx} - L_{mx}^2}{L_{rx}} \hat{i}_{sx\beta} \\ \hat{\phi}_{sx} = \sqrt{\hat{\phi}_{sx\alpha}^2 + \hat{\phi}_{sx\beta}^2} \\ \hat{\theta}_{sx} = \tan^{-1} \left( \frac{\hat{\phi}_{sx\beta}}{\hat{\phi}_{sx\alpha}} \right) \end{cases}, \quad (20)$$

$$\hat{T}_{emx} = \frac{5P_x}{2} (\hat{\phi}_{sx\alpha} \hat{i}_{sx\beta} - \hat{\phi}_{sx\beta} \hat{i}_{sx\alpha}), \quad (21)$$

The estimated electromagnetic torque and measured load torque, allow to calculate the rotor mechanical speed of the machine.

$$\hat{\omega}_{mx} = \frac{1}{J_x} \int (\hat{T}_{emx} - T_{lx} - f_x \hat{\omega}_{mx}) dt, \quad (22)$$

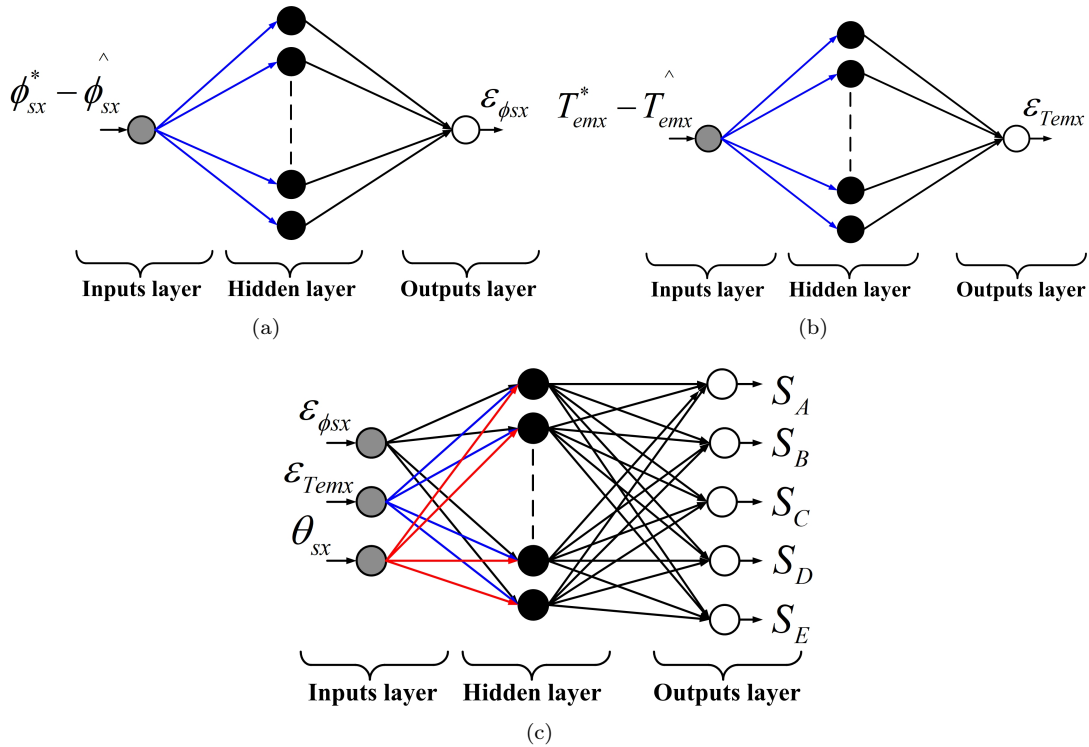


Fig. 6: Structure of the implemented ANN controllers: (a) ANN-HC $_{\phi_s}$ , (b) ANN-HC $_{T_{em}}$  and (c) ANN-ST.

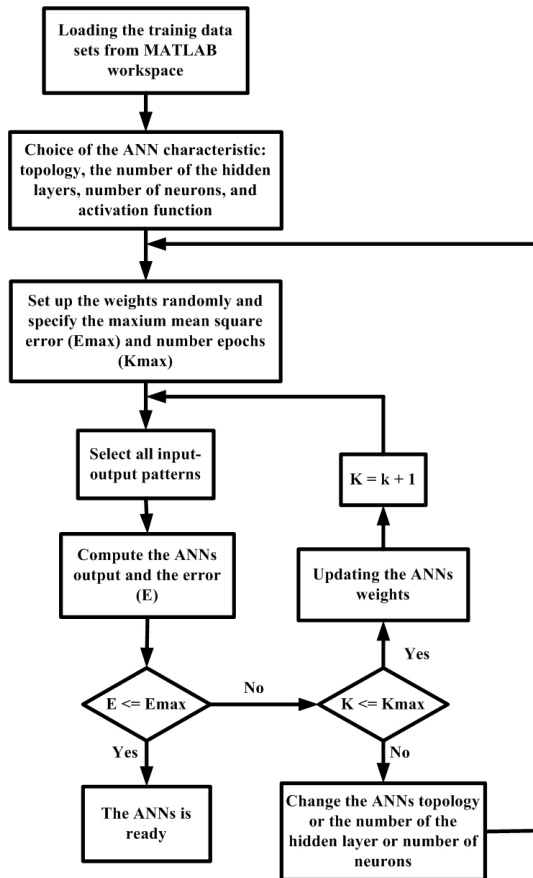


Fig. 7: The flow chart of the Back-propagation training algorithm.

## 6. Simulation results and discussion

Two different simulation tests are carried out in MATLAB/SIMULINK software for the two control strategies, DTC and DTC-ANN, to analyze and evaluate the drive system’s performance. Due to the five-phase symmetry of the FPIM, only phase "a" measured and reconstructed is presented. In this study, a post-fault operation is considered for the DTC-ANN scheme. Figures 10 to 19 illustrate the simulation results. The parameters of each machine are preset in Appendix A.

In this test, the robustness of the drive system is evaluated as the two machines run in opposite directions for low- and high-speed reference commands under their rated loading conditions. The speed reference for the FPIM1 is set to 1 rad/s, 20 rad/s, 100 rad/s, and -100 rad/s at instants  $t = 0.05s$ ,  $t = 1.1s$ ,  $t = 2.4s$ , and  $t = 4.5s$ , respectively. As for FPIM2, the reference commands are set to -100 rad/s, 1 rad/s, 20 rad/s, and 100 rad/s at instants  $t = 0.5s$ ,  $t = 2.05s$ ,  $t = 3.1s$ , and  $t = 4.4s$ , respectively.

This test examines a step variation in load torque to examine the robustness of the drive system in both motoring and generating modes. The speed reference for both machines is set to 100 rad/s at  $t = 0.5s$ . The load torque reference command for FPIM1 is set to 4 Nm at the start. Then, at instant  $t = 1s$ , the load

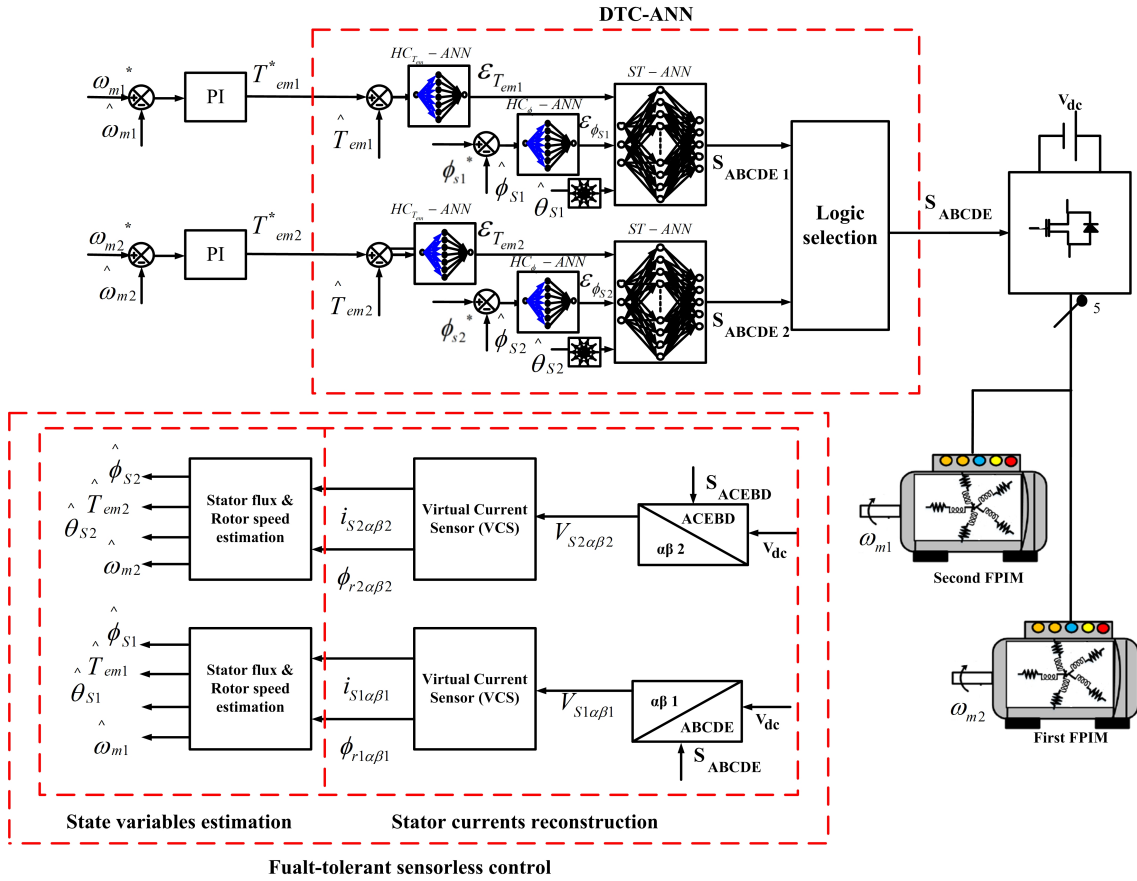


Fig. 8: Schematic diagram of three-level sensorless DTC-ANN for two parallel-connected FPIMs.

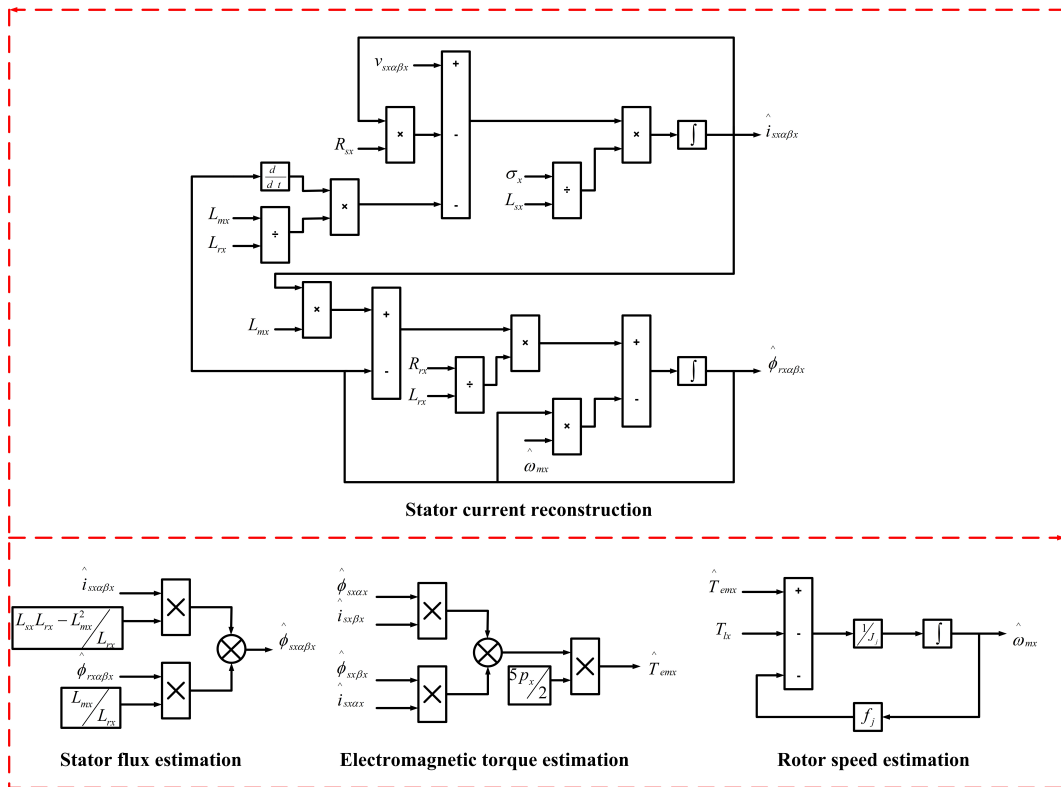


Fig. 9: FTC schematic diagram.



torque is set to -8 Nm. After that, at Instant  $t = 2.5s$ , the load torque is removed. As for the FPIM2, it starts at no load condition, then at  $t = 1.5s$ , a step change in load torque of 6 Nm is introduced. After that, at instant  $t = 3.5s$ , the load torque is set to -4 Nm.

Figure 10 and Figure 14 illustrate the stator flux trajectory in the  $\alpha - \beta$  of the two machines for DTC and DTC-ANN methods. From the present results, the stator flux of the two motors follows their reference values independently of the operating conditions in a circular trajectory. The DTC-ANN has greatly reduced the stator flux ripples by 46% compared to DTC. However, the DTC showed a better and more steady response at the start than the DTC-ANN.

Figure 11 and Figure 15 depict the electromagnetic torque response of the two FPIMs for the two control schemes under different operating scenarios. Compared to DTC, the DTC-ANN presents a better dynamic response in terms of ripple reduction by 45% and torque error both in transient and steady-state, as well as the motoring and generating operation.

The two machines' rotor speed responses are shown in Figure 12 and Figure 16. The simulation tests were carried out for different speed reference commands, and under constant and sudden changes in loading conditions, the two machines' speeds complied with their reference values with negligible over/undershoots due to the application or removal of the load torque.

According to Figure 13 and Figure 17, the phase "a" stator currents of the two FPIMs present a high content of ripples (harmonic currents), which are significantly reduced in the discussed DTC-ANN method.

Figure 18 and Figure 19 show the FFT analysis of phase "a" stator currents of the two FPIMs for the DTC and DTC-ANN schemes under the same operating conditions. It can be noticed that the DTC-ANN technique scientifically reduced the harmonic content in the stator current by 10% compared to DTC.

Finally, the reconstructed stator currents and estimated rotor speed in the DTC-ANN method obtained by the sensorless algorithm, presented in Figures 20 and 21, respectively, present an excellent estimation quality for different operating scenarios such as low-speed operation, step variation of load torque, and motoring and generating mode operation with negligible error.

From the presented results, the DTC-ANN outperforms the DTC method while preserving the latter's advantages. Moreover, the parallel-connected two-machine drive's independence, robustness, and stability are verified and ensured for different operating scenarios, even for post-fault operation.

Table 3 gives a summarized comparison between the two controls studied in this paper.

## 7. Conclusion

This paper investigates a three-level voltage source inverter fed a parallel-connected two FPIMs drive system using direct torque control based on artificial neural network DTC-ANN. The validation results demonstrate the robustness of the proposed sensorless DTC-ANN in transient and steady-state, in large speed range operation and load variation. Moreover, reduction of the stator flux, electromagnetic torque ripples, and stator current THD is achieved. In addition, the virtual current sensor algorithm is included to form fault tolerant control in the case of current sensor failure.

## Author Contributions

The idea for this paper was conceived by the authors of this work, with Benyoussef and add Tabbache. supervising the work. Benzaoui and Guedida collaborated on the design of the artificial neural network-based DTC for the two parallel connected drive. Benzaoui, Guedida, add Tabbache Bekheira, and Kouache contributed to the writing of the manuscript, while Tabbache Bekheira and Benyoussef provided crucial feedback and approved the final version for submission.

## References

- [1] LEVI, E. Multiphase electric machines for variable-speed applications. *IEEE Transactions on industrial electronics*. 2008, vol. 55, iss. 5, pp. 1893–1909. ISSN 0278-0046. DOI: 10.1109/TIE.2008.918488.
- [2] NESRI, M., K. NOUNOU, G. SIFELISLAM, M.F. BENKHORIS and H. AZEDDINE. Hybrid Flatness-Based Control of Dual Star Induction Machine Drive System for More Electrical Aircraft. *Power Electronics and Drives*. 2024, vol. 9, iss. 1, pp. 50–62. ISSN 2543-4292. DOI: org/10.2478/pead-2024-0004.
- [3] NESRI, M., H. BENKADI, K. NOUNOU, G. SIFELISLAM and M.F. BENKHORIS. Fault Tolerant Control of a Dual Star Induction Machine Drive System using Hybrid Fractional Controller. *Power Electronics and Drives*. 2024, vol. 9, , iss. 1 pp. 161-175. ISSN 2543-4292. DOI: 10.2478/pead-2024-0010.

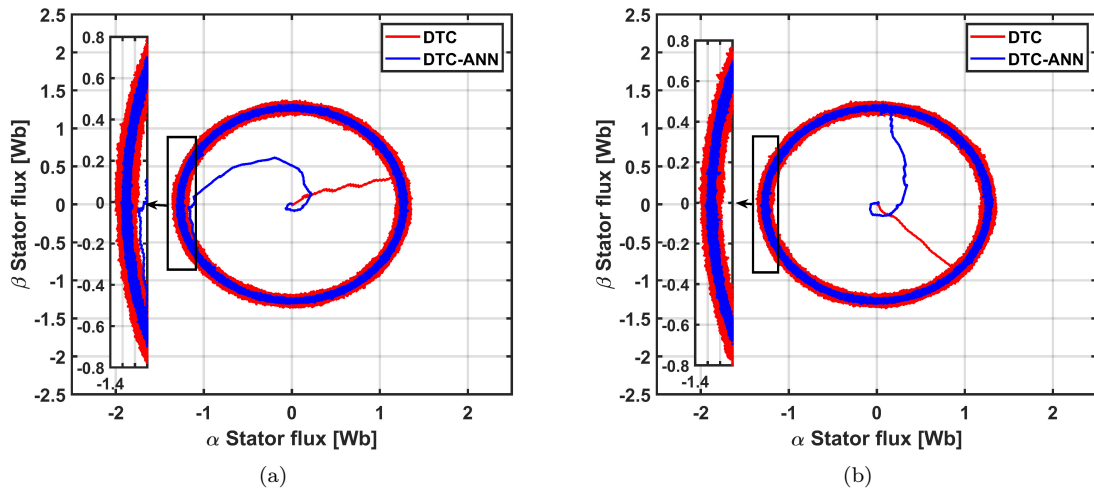


Fig. 10: Stator flux trajectory: (a) FPIM1 and (b) FPIM2.

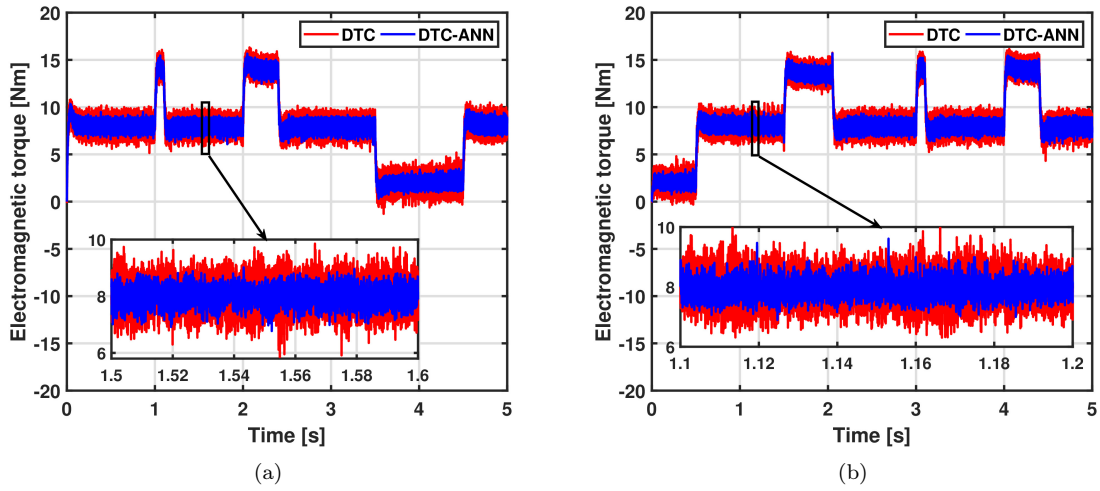


Fig. 11: Electromagnetic torque response: (a) FPIM1 and (b) FPIM2.

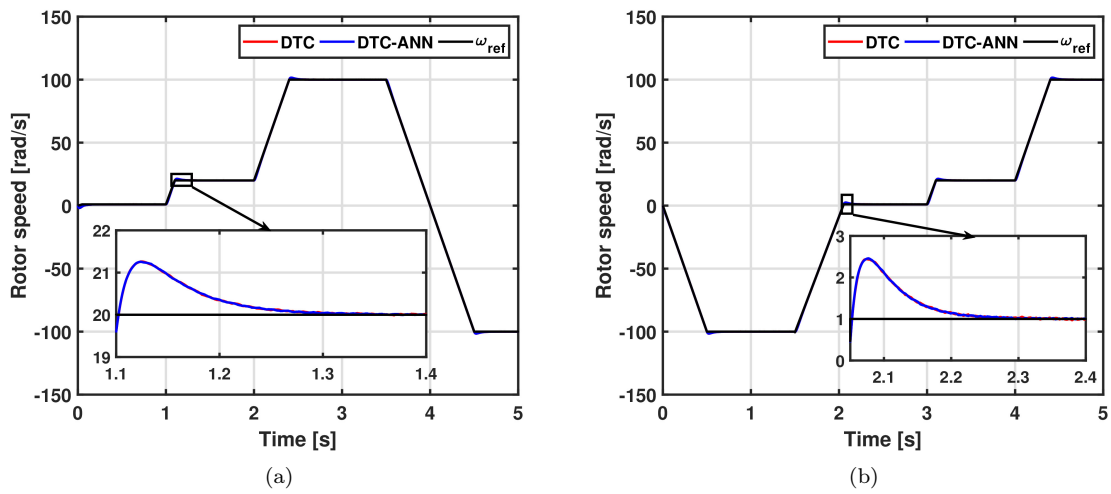


Fig. 12: Rotor speed response: (a) FPIM1 and (b) FPIM2.

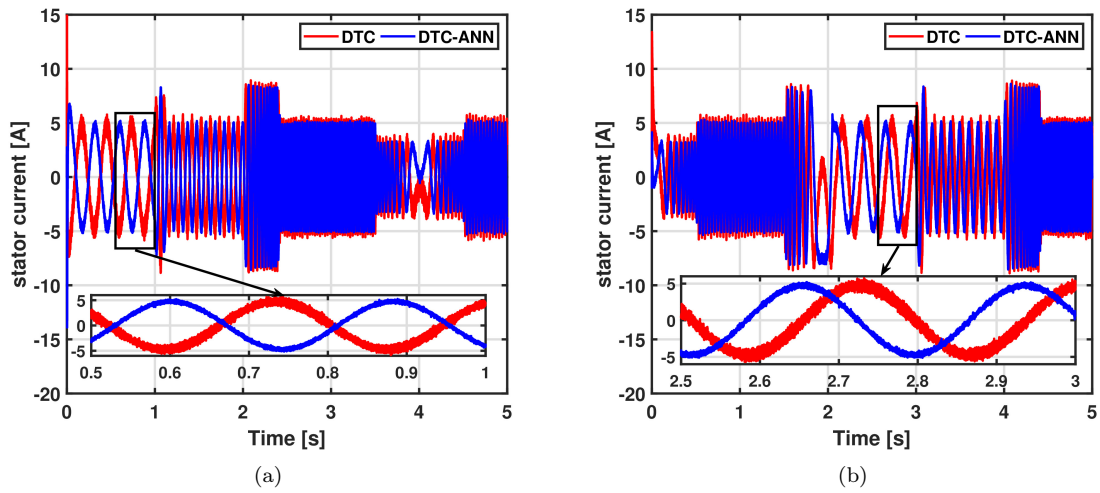


Fig. 13: Phase “a” stator current: (a) FPIM1 and (b) FPIM2.

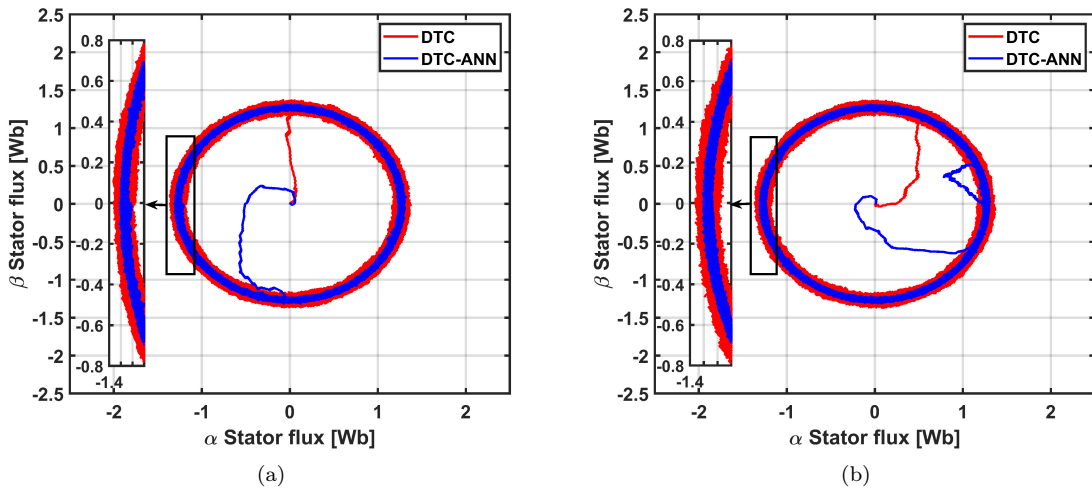


Fig. 14: Stator flux trajectory: (a) FPIM1 and (b) FPIM2.

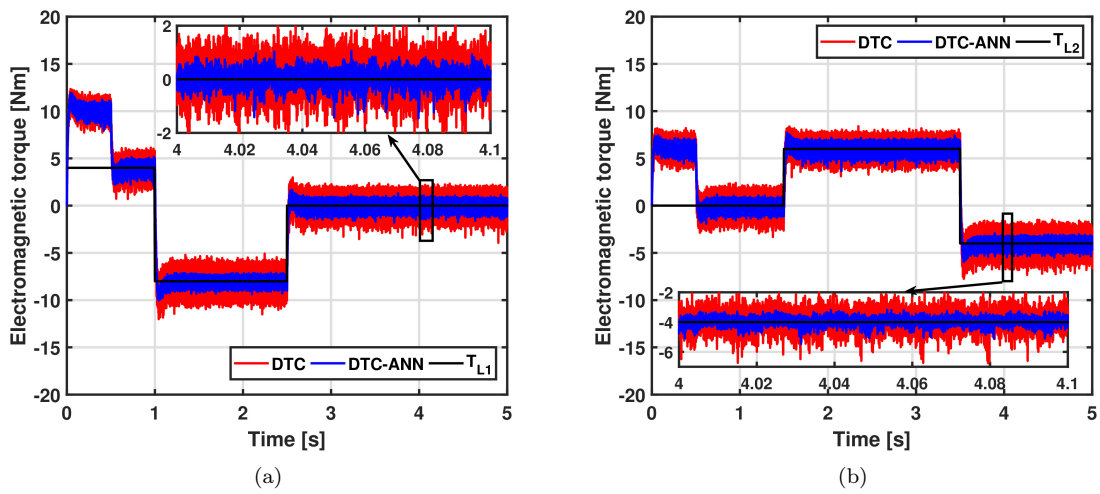


Fig. 15: Electromagnetic torque response: (a) FPIM1 and (b) FPIM2.

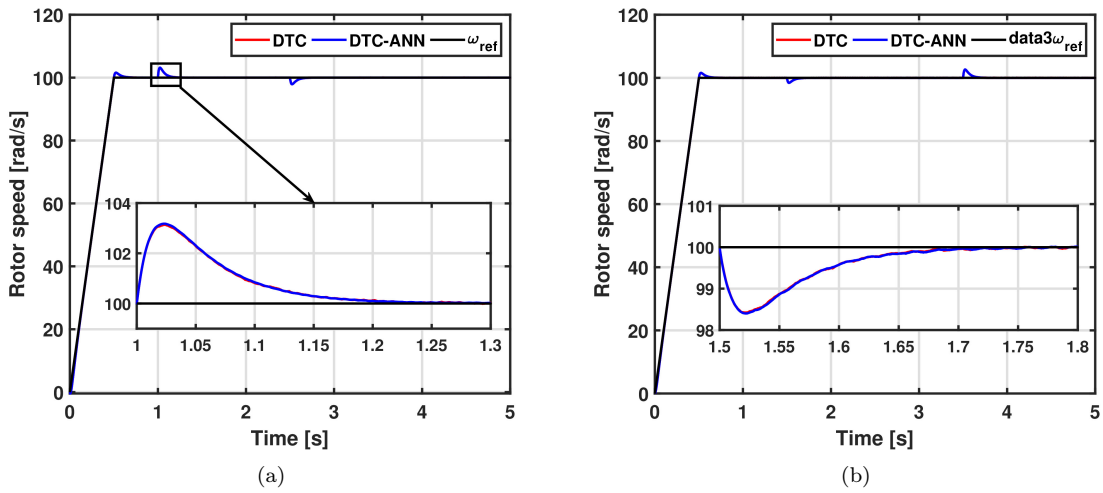


Fig. 16: Rotor speed response: (a) FPIM1 and (b) FPIM2.

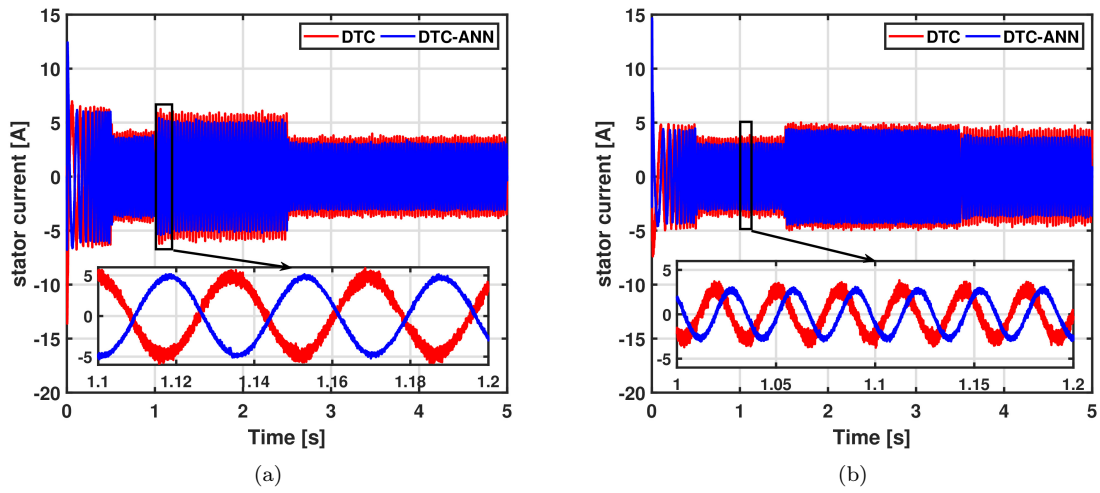


Fig. 17: Phase "a" stator current: (a) FPIM1 and (b) FPIM2.

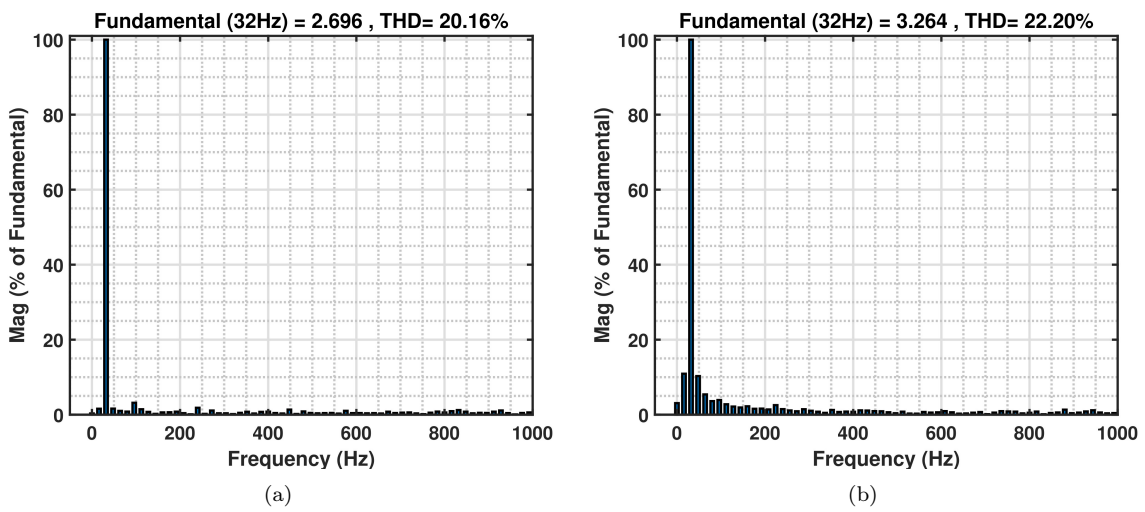


Fig. 18: Phase "a" stator current THD in DTC: (a) FPIM1 and (b) FPIM2.

Tab. 3: Comparative analysis of classical DTC and Proposed DTC-ANN.

| Performance | Assessment parameters |            | FPIM1  |         | FPIM2  |         |
|-------------|-----------------------|------------|--------|---------|--------|---------|
|             |                       |            | DTC    | DTC-ANN | DTC    | DTC-ANN |
| $\omega_m$  | Recovery time (s)     |            | 0.13   | 0.13    | 0.13   | 0.13    |
|             | Overshoot (rad/s)     |            | 0.8    | 0.8     | 0.8    | 0.8     |
|             | Undershoot (rad/s)    |            | 0.8    | 0.8     | 0.8    | 0.8     |
| $T_{em}$    | Ripples (Nm)          | High-speed | 3.2513 | 2.5169  | 3.1101 | 2.2814  |
|             |                       | Low-speed  | 3.3512 | 2.3209  | 3.1560 | 2.2373  |
| $\phi_s$    | Ripples (wb)          | High-speed | 0.1986 | 0.0892  | 0.1984 | 0.0914  |
|             |                       | Low-speed  | 0.1919 | 0.0856  | 0.2000 | 0.0881  |
| $i_{sa}$    | THD (%)               |            | 20.16  | 7.84    | 22.2   | 12.96   |

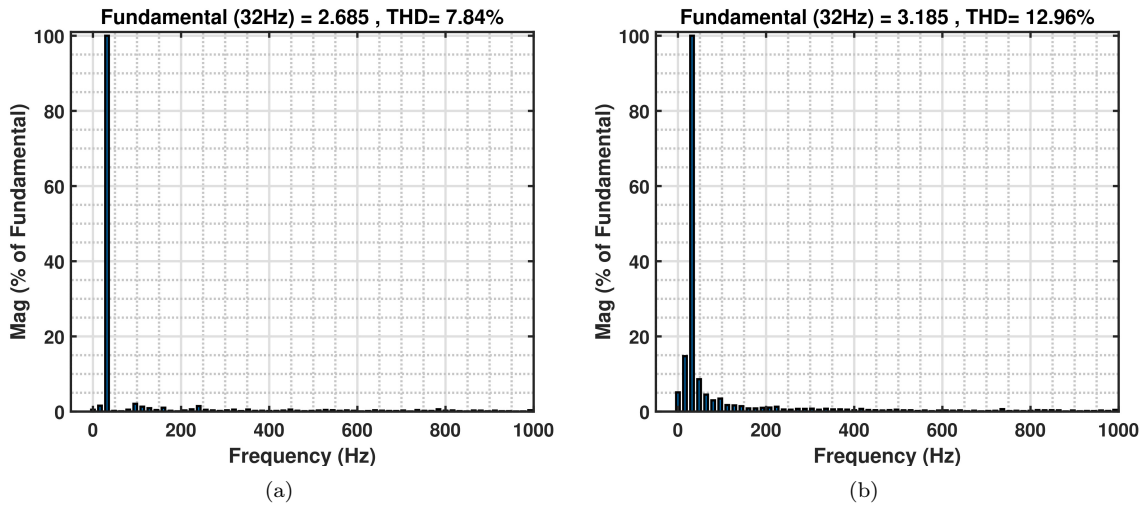


Fig. 19: Phase “a” stator current THD in proposed DTC-ANN: (a) FPIM1 and (b) FPIM2.

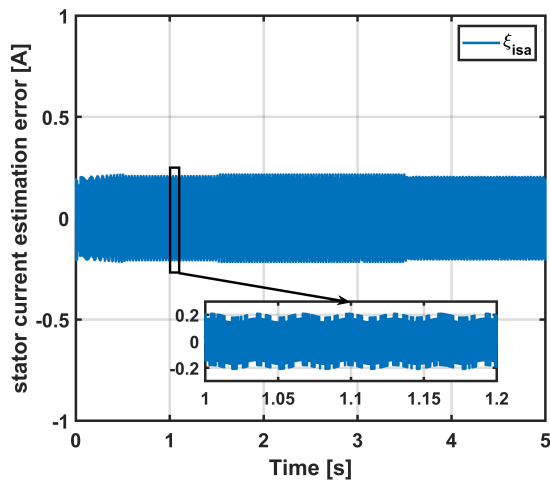


Fig. 20: Stator current estimation error.

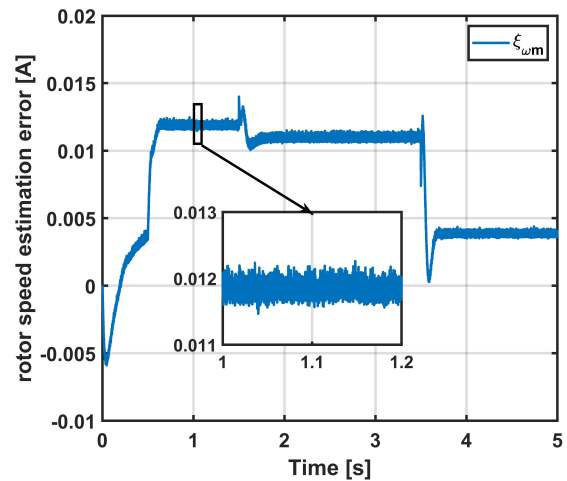


Fig. 21: Rotor speed estimation error.



- [4] SAADEH, O., M. DALBAH and Z. DALALA. Control of two Five-Phase Parallel Connected Single Source Motor Drives under Balanced and Unbalanced Conditions. In: *2018 9th IEEE International Symposium on Power Electronics for Distributed Generation Systems (PEDG)*. USA: IEEE, 2018, pp. 1–6. DOI: 10.1109/PEDG.2018.8447807.
- [5] KAMEL, T., D. ABDELKADER, B. SAID, M.F. AL HITHMI and A. IQBAL. Sliding mode control based dtc of sensorless parallel-connected two five-phase pmsm drive system. *Journal of Electrical Engineering and Technology*. 2018, vol. 13, iss. 3, pp. 1185-1201. ISSN 2093-7423. DOI: org/10.5370/JEET.2018.13.3.1185.
- [6] KAMEL, T., D. ABDELKADER, B. SAID, S. PADMANABAN and A. IQBAL. Extended Kalman filter based sliding mode control of parallel-connected two five-phase PMSM drive system. *Electronics*. 2018, vol. 7, iss. 2, pp. 14. ISSN 2079-9292. DOI: org/10.3390/electronics7020014.
- [7] KELLNER, J. and D. PRAŽENICA. Two five-phase induction motors used as an electronic differential. *Transportation Research Procedia*. 2021, vol. 55, pp. 896-903. ISSN 2352-1465. DOI: org/10.1016/j.trpro.2021.07.058.
- [8] JONES, M., E. LEVI and S. N. VUKOSAVIC. Independent Control of Two Five-Phase Induction Machines Connected in Parallel to a Single Inverter Supply. In: *IECON 2006 - 32nd Annual Conference on IEEE Industrial Electronics*. France: IEEE, 2006, pp. 1257-1262. DOI: 10.1109/IECON.2006.348152.
- [9] SAMBHAVI, Y. V. and V. RAMACHANDRAN. A technical review of modern traction inverter systems used in electric vehicle application. *Energy Reports*. 2023, vol. 10, pp. 3882-3907. ISSN 2352-4847. DOI: org/10.1016/j.egy.2023.10.056.
- [10] TAKAHASHI, I. and T. NOGUCHI. A New Quick-Response and High-Efficiency Control Strategy of an Induction Motor. *IEEE Transactions on Industry Applications*. 1986, vol. IA-22, iss. 5, pp. 820-827. ISSN 0093-9994. DOI: 10.1109/TIA.1986.4504799.
- [11] TATTE, Y., M. AWARE and C. KHADSE. Torque ripple reduction in three-level five-phase inverter-fed five-phase induction motor. *Electrical Engineering*. 2022, vol. 104, iss. 6, pp. 3793-3805. ISSN 1432-0487. DOI: org/10.1007/s00202-022-01579-4.
- [12] GUEDIDA, S., B. TABBACHE, K. NOUNOU and M. BENBOUZID. Direct Torque Control Scheme for Less Harmonic Currents and Torque Ripples for Dual Star Induction Motor. *Revue Roumaine Des Sciences Techniques—Série Électrotechnique Et Énergétique*. 2023, vol. 68, iss. 4, pp. 331-338. ISSN 0035-4066. DOI: org/10.59277/RRST-EE.2023.4.2.
- [13] GUEDIDA, S., B. TABBACHE, K. NOUNOU and A. IDIR. Reduced-order fractionalized controller for disturbance compensation-based on direct torque control of DSIM with less harmonic. *Electrica*. 2024, vol. 24, iss. 2, pp. 450-462. ISSN 2619-9831. DOI: 10.5152/electrica.2024.23194.
- [14] GDAIM, S., A. MTIBAA and M. F. MI-MOUNI. Artificial neural network-based DTC of an induction machine with experimental implementation on FPGA. *Engineering Applications of Artificial Intelligence*. 2023, vol. 121, pp. 105972. ISSN 1873-6769. DOI: org/10.1016/j.engappai.2023.105972.
- [15] GHAMRI, A., R. BOUMAARAF, M. T. MESLOUB, H. GOLEA and N. GOLEA. Comparative study of ANN DTC and conventional DTC controlled PMSM motor. *Mathematics and Computers in Simulation*. 2020, vol. 167, pp. 219-230. ISSN 1872-7166. DOI: org/10.1016/j.matcom.2019.09.006.
- [16] ZEGAI, M. L., M. BENDJEBBAR, K. BELHADRI, M. DOUMBIA, M. B. HAMANE and P. M. KOUMBA. Direct torque control of Induction Motor based on artificial neural networks speed control using MRAS and neural PID controller. In: *2015 IEEE Electrical Power and Energy Conference (EPEC)*. Canada: IEEE, 2015, pp. 320-325. DOI: 10.1109/EPEC.2015.7379970.
- [17] BANDA, G. and S. G. KOLLI. An intelligent adaptive neural network controller for a direct torque controlled eCAR propulsion system. *World Electric Vehicle Journal*. 2021, vol. 12, iss. 1, pp. 44. ISSN 2032-6653. DOI: org/10.3390/wevj12010044.
- [18] KAMEL, T. L., D. ABDELKADER, B. SAID and A. IQBAL. Direct torque control based on artificial neural network of a five-phase PMSM drive. In: *Artificial Intelligence in Renewable Energetic Systems: Smart Sustainable Energy Systems*. Springer, 2018, pp. 316-325. DOI: org/10.1007/978-3-319-73192-6\_33.
- [19] ADAMCZYK, M. and T. ORLOWSKA-KOWALSKA. Influence of the stator current

- reconstruction method on direct torque control of induction motor drive in current sensor postfault operation. *Bulletin of the Polish Academy of Sciences: Technical Sciences*. 2022, vol. 70, iss. 1, pp. 140099. ISSN 2300-1917. DOI: 10.24425/bpasts.2022.140099.
- [20] DYBKOWSKI, M. L., K. KLIMKOWSKI and T. ORLOWSKA-KOWALSKA. Speed and current sensor fault-tolerant-control of the induction motor drive. In: *Advanced Control of Electrical Drives and Power Electronic Converters*. Springer, 2017, pp. 141-167. DOI: org/10.1007/978-3-319-45735-2\_7.
- [21] SON, Y. and J. KIM. A novel phase current reconstruction method for a three-level neutral point clamped inverter (NPC) with a neutral shunt resistor. *Energies*. 2018, vol. 11, iss. 10, pp. 2616. ISSN 1996-1073. DOI: org/10.3390/en11102616.
- [22] JIANG, C. L., H. LIU and D. CHEN. A Novel five phase current reconstruction technique fed by dual inverter. In: *2020 International Conference on Electrical Engineering and Control Technologies (CEEECT)*. Australia: IEEE, 2020, pp. 320-325. DOI: 10.1109/CEEECT50755.2020.9298620.
- [23] RONANKI, D., K. R. PITTAMK., A. DEKKA, P. PERUMAL and A. R. BEIG. Phase Current Reconstruction Method With an Improved Direct Torque Control of SRM Drive for Electric Transportation Applications. *IEEE Transactions on Industry Applications*. 2022, vol. 58, iss. 6, pp. 7648-7657. ISSN 0093-9994. DOI: 10.1109/TIA.2022.3196329.
- [24] TATTE, Y. N. and M. V. AWARE. Torque ripple and harmonic current reduction in a three-level inverter-fed direct-torque-controlled five-phase induction motor. *IEEE Transactions on Industrial Electronics*. 2017, vol. 64, iss. 7, pp. 5265-5275. ISSN 0278-0046. DOI: 10.1109/TIE.2017.2677346.
- [25] GUEDIDA, S., B. TABBACHE, K. M. S. BENZAOU, K. NOUNOU. and M. NESRI. Novel Speed Sensorless DTC Design for a Five-Phase Induction Motor with an Intelligent Fractional Order Controller Based-MRAS Estimator. *Power Electronics and Drives*. 2024, vol. 9, iss. 1, pp. 63-85. ISSN 2543-4292. DOI: 10.2478/pead-2024-0005.
- [26] BIÇAK, A. and A. GELEN. Sensorless direct torque control based on seven-level torque hysteresis controller for five-phase IPMSM using a sliding-mode observer. *Engineering Science and Technology, an International Journal*. 2021, vol. 24, iss. 5, pp. 1134-1143. ISSN 2215-0986. DOI: org/10.1016/j.jestch.2021.02.004.
- [27] BENZAOU, K. M. S., E. BENYOUSSEF. and A. Z. KOUACHE. 'Stator Flux and Speed Sensorless Control for DTC-ANN of Two Parallel-Connected Five-Phase Induction Machines Based on Sliding Mode Observer. *Majlesi Journal of Electrical Engineering*. 2024. DOI: 10.30486/mjee.2024.2007701.1374.

## Appendix A The parameters of two FPIMs

- $V_n = 200 \text{ V}$ ,
- $I_n = 5 \text{ A}$ ,
- $R_s = 10 \Omega$ ,
- $R_r = 6.3 \Omega$ ,
- $L_s = 0.4642 \text{ H}$ ,
- $L_r = 0.4612 \text{ H}$ ,
- $L_m = 0.4212 \text{ H}$ ,
- $j = 0.03 \text{ Kg.m}^2$ ,
- $f = 0.0001 \frac{\text{Nm.s}^{-1}}{\text{rad}}$ ,
- $T_{em} = 8 \text{ N.m}$ ,
- Step time =  $10^{-5} \text{ Sec}$ ,
- Average switching frequency =  $8 \text{ KHz}$ ,
- $P = 2$ .